2010-06-25

Piezoresistive Nano-Composites: Characterization and Applications

Thomas B. Hyatt
Brigham Young University - Provo

Piezoresistive Nano-Composites: Characterization and Applications

Tommy Hyatt

A thesis submitted to the faculty of
Brigham Young University
in partial fulfillment of the requirements for the degree of

Master of Science

David T. Fullwood, Chair
A. Brent Strong
Anton E. Bowden

Department of Mechanical Engineering

Brigham Young University

August 2010

ABSTRACT

Piezoresistive Nano-Composites: Characterization and Applications

Tommy Hyatt

Department of Mechanical Engineering

Master of Science

Innovative multifunctional materials are essential to many new sensor applications. Piezoresistive nano-composites make up a promising class of such materials that have the potential to provide a measurable response to strain over a much wider range than typical strain gages. Commercial strain gages are currently dominated by metallic sensors with a useable range of a few percent strain at most [1]. There are, however, many applications that would benefit from a reliable wide-range sensor. These might include the study of explosive behavior, instrumentation of flexible components, motion detection for compliant mechanisms and hinges, human-technology interfaces, and a wide variety of bio-mechanical applications where structural materials may often be approximated as elastomeric.

In order to quantify large strains, researchers often use optical methods which are tedious and difficult. This thesis proposes a new material and technique for quantifying large strain (up to 40%) by use of piezoresistive nano-composite strain gages. The nano-composite strain gage material is manufactured by suspending nickel nano-strands within a biocompatible silicone matrix. Study and design iteration on the strain gage material requires an improved understanding of the electrical behavior and conduction path within the material when strained. A percolation model has been suggested for numerical approximations, but has only provided marginal results for lack of data. Critical missing information in the percolation model is the nano-strand cluster size, and how that size changes in response to strain. These data are gathered using a dynamic technique in the scanning electron microscope called voltage contrast. Cluster sizes were found to vary in size by approximately 6% upon being strained to 10%.

A feasibility study is also conducted on the nano-composite to show its usability as a strain gage. High Displacement Strain Gages (HDSGs) were manufactured from the nano-composite. HDSGs measured the strain of bovine ligament under prescribed loading conditions. Results demonstrate that HDSGs are an accurate means for measuring ligament strains across a broad spectrum of applied deformations.

Keywords: Tommy Hyatt, nano-composite, quantum tunneling, bio mechanics, strain gage, optical marker tracking, OMT, electron microscope, SEM, voltage contrast, percolation

ACKNOWLEDGMENTS

I gratefully acknowledge the outstanding help I have received from the many people who have stood by me in this academic journey. To my committee, thank you for the mentorship, advice, and open office doors for me to drop in. To Kevin Cole, thank you for always being willing to provide feedback on experimental set-up plans and especially for spending the entire Christmas break rewriting labview code for data capture. To my beautiful wife, Elizabeth, thank you for putting up with the long hours, for making sure I eat during the day, and for the sincere love I feel every day of my life. I am truly blessed by everyone around me.

TABLE OF CONTENTS

LIST OF TABLES

LIST OF FIGURES

1 WIDE RANGE STRAIN SENSING AND MULTIFUNCTIONAL MATERIALS

The ability to accurately measure strain is crucial to innumerable applications in industry and research. Since being invented in 1938, strain gages have dominated the strain sensing market due to their ease of use, and high accuracy. Standard strain gages, however, are only able to measure small strains. This limitation is the result of the physical properties of the piezoresistive materials used in the construction of the strain gages. Commercial strain gages are typically constructed of natural piezoresistors such as metals or ceramics. These materials deform plastically or otherwise fail when subjected to strain beyond 1% or 2% [1].

When strains above a few percent need to be quantified, alternate methods can be used, but these have significant drawbacks that must be dealt with. Alternate strain measurement techniques frequently employ optical methods, which require specialized equipment, and significant data processing. Applications requiring large strain measurement might include the study of explosives, inflatables, structures that deform plastically, and a vast array of biomechanical applications. By far, it would be preferable to simply have a strain gage capable of enduring large strains. Efforts in this direction have yielded only marginal results – piezoresistive polymers have been shown to be capable of larger deformations, but have not been able to provide accurate or repeatable results [2-4].

New advances in multifunctional materials and nanotechnology have enabled the creation of synthetically piezoresistive nano-composites. Specifically, a nano-composite material composed of silicone reinforced by nickel nano-strands and discontinuous nickel coated carbon

fiber has been proposed as a high displacement strain gage material. The nickel nano-strands are created by a proprietary chemical vapor deposition (CVD) process that yields nickel filaments with very high aspect ratios. The reinforcements are dispersed in the matrix using a low-shear planetary-centrifugal mixer, and cast into a thin sheet.

The unique electrical behavior of this material is attributed to an effect called quantum tunneling, which occurs when there exists a thin insulator between two conductors with a potential difference [5, 6]. While this non-intuitive effect facilitates a change in resistance throughout deformation (and thus allowing this material to be used as a strain gage), quantum tunneling creates modeling difficulties. Specifically, the changing size of the electrically connected nano-strand cluster becomes difficult to quantify and therefore difficult to model.

A novel application of an electron microscopy failure analysis technique is presented as a method for detecting electrically connected clusters. Electron images of conductive nano-composites are taken with and without an applied voltage, and the differences in the images are quantified and correlated to conduction clusters. These image results indicate that the electrically connected nickel nano-strand cluster size varies by approximately 6% throughout strain of 10%. Results using this technique will lead to an accurate percolation model which can be used to compare theoretical results with actual measured results.

To demonstrate one practical application of the nano-composite as a strain gage capable of large and repeated deformations, a test on biological tissue was conducted. Bovine ligament was repeatedly strained, which strain was measured by optical methods and the nano-composite High Displacement Strain Gage (HDSG) simultaneously. Results show that the HDSGs can measure strain in one dimension with greater than 90% accuracy.

2 CHARACTERIZATION

2.1 Manufacturing

In order to improve the understanding of a composite, it is instrumental first to understand the materials and the manufacturing process. The nano-composite being studied consists of three components: 1) Silicone – Dow Corning's® Sylgard 184, 88% by volume, 2) Nickel nano-strands – produced by Conductive Composites Company, LLC, 9% by volume, and 3) Chopped nickel coated carbon fibers – produced by Conductive Composites Company, LLC, 3% by volume, approximately 2mm in length. These components were combined using a THINKY brand planetary-centrifugal mixer because it has been shown to achieve excellent dispersion with very low shear forces, which serves to preserve the high aspect ratios of the relatively delicate nickel nano-strands. The prepared mixture is then cast into a thin sheet and cured under vacuum. [5]

2.2 Electrical Behavior

The nano-composite being studied exhibits piezoresistivity, which is to say, the measured resistance changes in response to an applied strain. This result is non-intuitive considering the insulating nature of the silicone matrix. Additionally, contrary to the behavior of natural piezoresistors, the resistance measured in the nano-composite *decreases* in response to strain. One might be inclined to think this behavior is due to increased electrical contact of the conductive reinforcements, but this is only partially correct. The reinforcements do indeed assist

in the changing conductivity, but they do not come into contact when the material is strained. The reinforcements are not in electrical contact, and straining the material does not cause new contact between conductors. The change in resistance is due to quantum tunneling.

Quantum tunneling is a result of the quantum mechanical behavior of electrons. As an electron wave packet approaches a potential energy barrier (such as an insulator), the solution to Schroedinger's equation predicts that the probability of finding an electron inside the potential barrier decays exponentially to zero with distance past the surface of the barrier. That means there is a *non-zero* possibility that the electron can travel *through* very thin barriers [6].

The nickel nano-strands come into very close proximity at numerous locations due to the highly branched structure and large aspect ratio. All of these locations are possible quantum tunneling sites (hereafter referred to as junctions). When the nano-composite is strained, the silicone matrix undergoes Poisson thinning, thus reducing the magnitude of the potential energy barrier at the quantum tunneling junctions. As previously mentioned, the probability of tunneling through a barrier increases exponentially with decreasing thickness. We can therefore expect the passage of electrons to change exponentially with strain (if Poisson thinning is assumed to be linear with strain).

The overall conductivity of the nano-composite obviously depends on the relative volume of conductive reinforcements. On the one hand, if enough nickel is added, the nano-composite will behave like a conductor, and will not exhibit a change in resistance in response to an applied deformation. On the other hand, if too little nickel is added, the nano-composite will behave like an insulator and will also fail to exhibit a change in resistance. The discontinuous carbon fibers are added in order to help linearize the electrical response and to improve uniformity. While it is convenient to assume that the nano-strand clusters are perfectly dispersed, the addition of the

carbon fibers greatly improves the uniformity of electrical connection between microclusters. This is because the Nickel coated carbon fibers connect nano-nickel clusters over relatively long distances, which modifies the percolative behavior, decreasing the percolation threshold, and thereby linearizing the response. Despite the non-homogeneous nature of the nano-composite at the micro scale, the feature size of the electrically conductive reinforcements is more than an order of magnitude smaller than the sample size. Therefore, at the macro scale, the nano-composite is considered to be electrically homogeneous.

2.3 Modeling

Percolation theory is being used to numerically model the electrical behavior of the nano-composite. In mathematics, percolation theory describes the behavior of connected clusters in a random arrangement in two or more dimensions [7]. This is particularly well suited for the nano-composite being discussed because the nickel nano-strand clusters are randomly oriented, and distributed throughout the volume. In percolation theory, the material properties in the region of the percolation threshold can be related to the average connected cluster size via well known scaling laws [8]. There are, however, critical data missing from the analysis that prevents the percolation model from becoming an accurate tool: the nano-strand cluster size and how that size changes in response to applied strain.

While the size of a single nano-strand can be determined handily, the size of an embedded nano-strand cluster is rather elusive. When preparing the composite, nano-strands can become tangled and experience classical contact in the finished nano-composite. Additionally, there is an equilibrium number of quantum tunneling junctions even when the nano-composite is unstrained. Finally, when the nano-composite is strained, new quantum tunneling junctions are

activated, which changes the cluster size. The result is clusters of unknown (and changing) size that are buried in opaque silicone.

Given that the cluster sizes cannot be measured directly, they must be measured indirectly. Cluster size is dependent on the size of classically connected conductive reinforcements and the number of quantum tunneling junctions. Attempts to analytically predict the average size of classically connected clusters cannot be verified, to say nothing of an inability to measure or count the number of quantum tunneling junctions per unit volume. The next obvious choice for cluster measurement is to apply a voltage and simply detect the size of the electrically connected area. One very effective method of visualizing areas that are (and are not) in electrical contact is called voltage contrast. This method has been used by the semiconductor industry for failure analysis purposes for decades [9]. Voltage contrast visualization can be achieved in several different ways, but each method requires the use of a scanning electron microscope [10].

2.4 Voltage Contrast

The scanning electron microscope (SEM) is a powerful and versatile tool, and has been used frequently in many different ways to generate contrast images. Voltage contrast imaging is possible when using an electron microscope to view samples that are conductive in some areas and nonconductive in others [10]. Using voltage contrast techniques, the electrically connected cluster size can be measured. The data from voltage contrast experiments will be used to analyze cluster size versus strain level and hence lead to an accurate percolation based model. In order to understand how the SEM can allow the observation of subsurface nano-strand clusters and why contrast images are developed, it becomes necessary to review the function of the SEM, and the various settings that can affect the electron beam and its interaction with the sample.

2.4.1 SEM Basic Function

A scanning electron microscope creates an image of a sample by firing electrons at it inside a vacuum. When the electron beam meets the sample surface, the electrons can do one of two things: the impinging electrons can pass near the atoms of the sample causing the release of

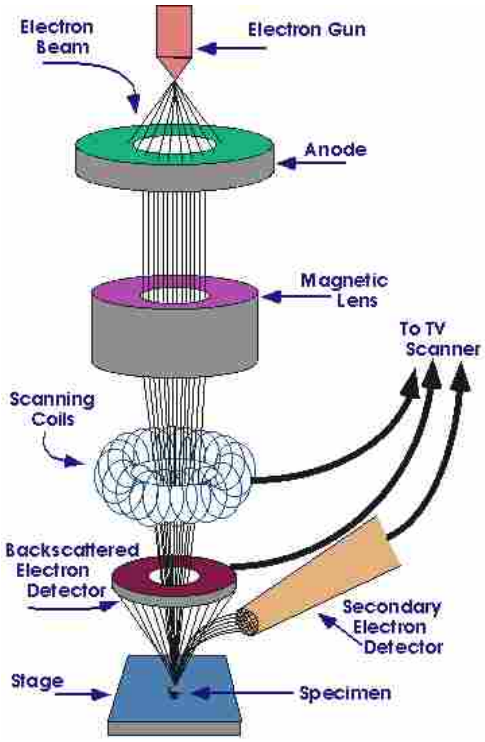

Figure 1 - Diagram of a SEM. Image courtesy of Microtech Sciences Limited.

'secondary electrons'; or they can impact an atom of the sample and bounce back as 'backscattered' electrons [11]. The electron gun 'fires' a continuous beam of electrons as it scans back and forth across the sample. Electron detectors and imaging software discretize the electron response, and then correlate the number of electrons collected at each discrete location with a grayscale value. Thus, if a large number of electrons are collected in a given location, the electron image in that location will appear brighter or even white. Likewise, if very few electrons are detected at some part of a sample, that part of the image will appear dark or even black. This

process occurs at all locations on the sample surface within the view field, and results in a grayscale image capable of resolving features so small that even the best optical microscopes could not hope to image [11].

Secondary electrons are produced when a primary electron passes close enough to an atom in the specimen to impart some of its energy to an orbital electron. If the orbital electron gains enough energy, it will break free of the host atom. When the orbital electron takes energy from the primary electron, the path of the primary electron will change slightly. The escaped orbital electron (now referred to as 'secondary') then leaves the atom with a very small kinetic energy (less than 50eV). If the secondary electron is near the sample surface (usually within about 100 angstroms), it can be ejected from the sample surface into the vacuum chamber. As the secondary electron has very little kinetic energy, its path can be easily influenced by an electrical field created by an applied potential. The electron detection system takes advantage of this fact by placing a faraday cage with a positive applied potential in front of the actual electron collector [12].

Backscattered electrons (BSEs) are produced when a primary electron collides with an atom in the sample. In this case, the primary electron bounces straight back without any appreciable energy loss. The number of BSEs produced depends directly on the atomic numbers of elements within the specimen. That is to say those elements with a high atomic number will create more BSEs, and will appear brighter whereas samples with low atomic numbers will create fewer BSEs and will appear darker. This behavior can be used to distinguish parts of the specimen that have differing average atomic number. The backscatter detector used to collect the BSEs is a solid state semiconductor device in the shape of an annulus and is mounted on the bottom of the column (see Figure 1). When BSEs reach the detector, electron-hole pairs are

created and counted. This quantity is given to the imaging software which determines the brightness of each pixel and goes on to form an image [11].

2.4.2 SEM Settings

The number of secondary electrons emitted (and therefore the image generated by the SEM) is affected by many variables and settings. The following is a description of several standard SEM settings that can be easily adjusted and controlled by the user, along with a short explanation regarding the effect it may have.

Spot Size

Spot size refers to the diameter of the electron beam at the surface of the sample, and is determined by the current in the condenser lens. A small spot size allows greater detail per unit area scanned, whereas a large spot size will tend to smooth over the fine surface details [11]. While a small spot size will provide better resolution, increasing the condenser lens current also serves to reduce the beam current and thereby reduces the total number of electrons available to interact with the specimen. When fewer primary electrons interact with the sample, fewer secondary and back scattered electrons become available to form an image. This weaker signal can be boosted electronically, but this will also result in increased electronic noise. As the signal to noise ratio becomes low, the resulting image becomes increasingly grainy [12].

Accelerating Voltage

The accelerating voltage is the high voltage applied to the anode just below the electron gun. When a small current is applied to the gun, a cloud of electrons will form. The electrons in this cloud will accelerate downwards in the presence of the field created by the high voltage. The

magnitude of accelerating voltages often used in SEM imaging varies between 1kV and 30kV. In general, increasing the accelerating voltage will increase the resolution. However, higher beam voltages create larger interaction volumes. When the interaction volume is larger, the area ejecting secondary electrons is larger, which serves to decrease resolution. This effect is more dramatic on samples with low atomic numbers such as polymers or biological samples [12].

Detector Bias

The detector bias is the relatively small positive potential applied to the faraday cage which attracts the low energy secondary electrons to the detector. Other electrons within the specimen chamber are not attracted by this low voltage and will only reach the detector if their direction of travel takes them to it. A higher detector bias will typically improve secondary electron collection efficiency, and therefore image resolution [11].

Tilt Angle

The tilt angle describes the angle at which a sample is tilted within the vacuum chamber relative to the incident electron beam. Tilting the sample causes the electron spot to cover more area and causes more of the interaction volume to be closer to the sample surface, both of which promote secondary electron emission. Collection efficiency is improved when positive tilt angles are used because secondary electrons that escape from the sample surface are already angled toward the detector [11].

Scan Rate

The scan rate refers to the speed at which the electron beam rasters across the viewing area. At high scan speeds, the beam does not dwell in any single location very long, so fewer

secondary electrons are emitted in each pass. This leads to a lower resolution 'grainy' picture, but can allow for nearly real-time focusing and shift of viewing area [11].

2.4.3 Voltage Contrast Techniques

Secondary electron images are the result of hundreds or thousands of pixels whose contrast is determined by the number of escaped and collected secondary electrons at each discrete location. If the number of escaping secondary electrons is modified in localized zones, the contrast in the resulting image will change. There are various ways to affect the electron yield of a sample independent of the SEM settings. A common phenomenon that affects secondary electron yield is electrical potential – a positive potential creates a field that will inhibit the escape of secondary electrons whereas a negative potential field will serve to expel secondary electrons. Several related techniques for utilizing this effect gained increasing popularity over the past 20 years [10, 13] - these imaging techniques (frequently referred to generally as "voltage contrast") can allow the visualization of areas that carry a voltage or current, and will be discussed briefly here.

Passive Voltage Contrast

Passive voltage contrast occurs when imaging electrically isolated samples that passively accumulate a net positive or negative charge. A net charge will accumulate if the number of escaping secondary electrons is not equal to the number of impinging primary electrons. Secondary electron yield can become greater than one when using low accelerating voltages (less than 2kV) because most of the secondary electrons that are generated will be close enough to the sample surface to escape, and a single primary electron is capable of generating several secondary electrons. The net positive surface charge will then compete with the faraday cage to

attract escaping secondary electrons [13]. As secondary electrons fail to reach the detector, the image will appear darker. Secondary electron yield becomes less than one when using higher accelerating voltages (greater than 2kV). With the greater accelerating voltage, there will be greater penetration, and therefore fewer secondary electrons near enough to the surface to be allowed to escape [13]. This results in a net negative charge which will then help to expel secondary electrons, allowing more to reach the detector resulting in a brighter image. When unintended, this effect is simply referred to as “charging” and can create much difficulty when viewing non-conductive samples [11].

Active Voltage Contrast

Active voltage contrast occurs when the SEM operator intentionally applies a positive or negative voltage to an electrically isolated sample being imaged. Areas with a positive applied potential will suppress the escape of secondary electrons and appear dark. Areas with a negative applied voltage will encourage the escape of secondary electrons and appear bright. This technique has become a popular failure analysis technique within the semi-conductor industry since the early 1990s [13] (see Figure 2).

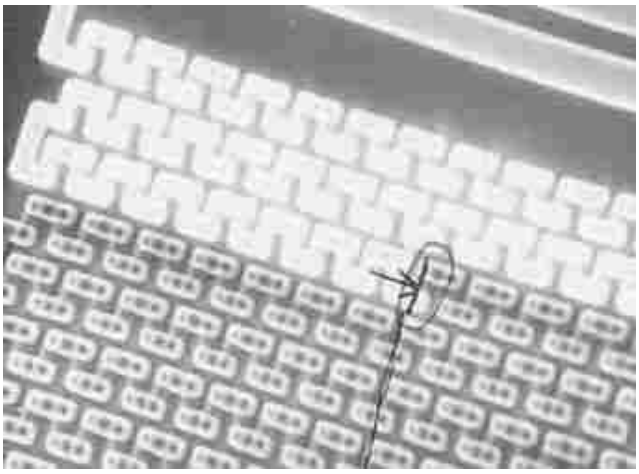

Figure 2 - Semiconductor failure identified using voltage contrast. Image courtesy of Accelerated Analysis.

Electron Beam Induced Current (EBIC)

EBIC is a technique developed for semiconductor analysis, which allows the SEM operator to identify buried junctions or defects in semiconductors. When electrons enter a semiconductor sample, the generation of secondary electrons also creates electron-hole pairs within the beam's interaction volume (a “hole” is simply the absence of an electron). If the sample contains a p-n junction, electron-hole pairs that are created at or near the junction's field may become separated. The separation will create a field which will cause electrons to flow to the n-side, and holes to the p-side. This net difference in charge can be detected using a picoammeter or current amplifier, thus allowing the separated electrons and holes to flow through the circuit. This current is described as having been induced by the electron beam. If the output of the current amplifier is used as the imaging signal of the SEM, EBIC microscopy is possible [6, 14, 15].

After reviewing the available techniques, Active Voltage Contrast was determined to be the most suited for visualizing nickel nano-strand clusters suspended in polymers.

2.5 Voltage Contrast on a T-O Can

To the knowledge of the author, active voltage contrast has never been performed on nano-composites. After developing an understanding of the governing physics, test samples were prepared and tested to demonstrate the viability of the proposed solution on the material being investigated. The simplest voltage contrast scenario considered required two discrete areas on a sample where one was subjected to an applied voltage, and the other was connected to ground. The sample selected is called a T-O can, and is where transistors are typically mounted. It consists of a disc which holds two electrically isolated pins in place (see Figure 3).

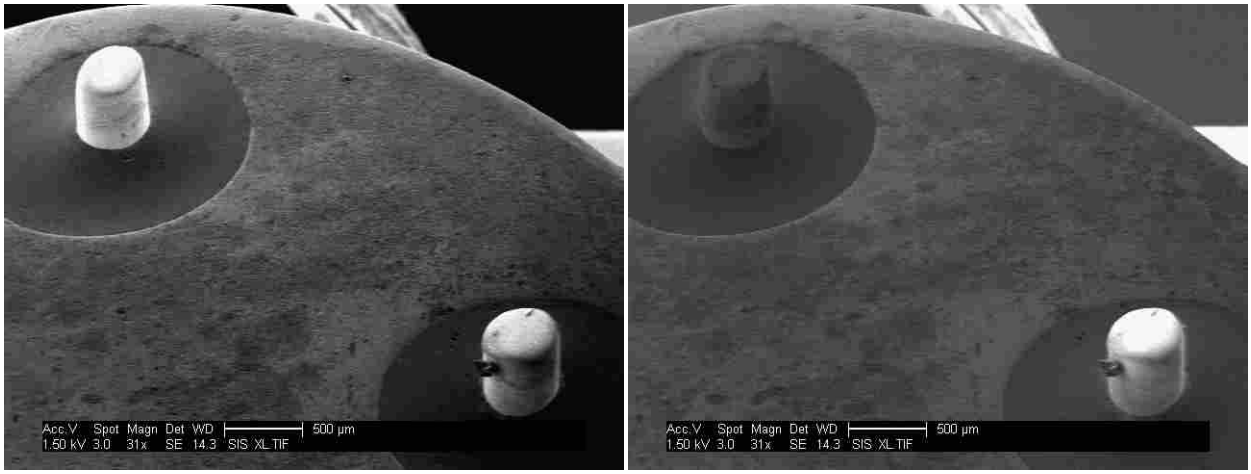

Figure 3 - Active Voltage Contrast on a T-O can. In the left image, the upper pin is grounded. In the right image, the upper pin has +40 VDC applied.

A T-O can was obtained, and mounted to a microscope stub such that one pin was in electrical contact with ground, and the other was connected to a wire that passed through the vacuum plane. Outside the vacuum chamber, this wire was connected to a DC voltage supply that was capable of applying plus or minus 40 volts. A positive voltage was applied, and the electron image changed as expected (see Figure 3).

2.6 Statistical Analysis

After demonstrating the technique at Brigham Young University (BYU), a statistical analysis was performed to optimize the SEM settings for creating voltage contrast images on nickel filled polymers. The SEM settings previously discussed here do not by any means represent an exhaustive list of variables that affect the SEM images, but they do represent the settings that are most commonly adjusted, and would be easily altered to fit our needs. The sample used in the statistical analysis was a CP1 (polyimide) film containing 15% nickel nano-strands by volume. This sample was selected because nickel nano-strands demonstrate excellent suspension in CP1, and CP1 cures to a hard solid that can be polished well. To ensure electrical

isolation from ground, the uncured polymer/nano-strand mixture was cast onto a 0.9” acrylic disk (0.125” thick). To provide a means for applying a potential, a thin copper wire was cast into place to ensure good electrical contact with the nickel nano-strands. Before viewing the cured sample, the surface was polished to expose some of the nickel nano-strands that were near the surface.

Based on what is known about the physics that govern voltage contrast, we expect to achieve good contrast when a relatively large number of secondary electrons are generated. This would allow the conductive areas of a sample to have the greatest effect on the resulting image. The settings described in Table 1 were implemented in a pre-determined random order, and an image was saved at each setting. The angle of tilt was held constant at 50 degrees.

Table 1 – Factorial Design for Analysis of SEM Settings

Standard Order	Voltage	Bias	Beam Voltage	Scan Rate	Spot Size
1	-40	0	1.5	slow	4
2	40	0	1.5	slow	2
3	-40	300	1.5	slow	2
4	40	300	1.5	slow	4
5	-40	0	5	slow	4
6	40	0	5	slow	2
7	-40	300	5	slow	2
8	40	300	5	slow	4
9	-40	0	1.5	TV	4
10	40	0	1.5	TV	2
11	-40	300	1.5	TV	4
12	40	300	1.5	TV	2
13	-40	0	5	TV	2
14	40	0	5	TV	4
15	-40	300	5	TV	2
16	40	300	5	TV	2

Each image was judged based on the quality of contrast achieved, and a numeric value on a scale from 1 to 10 was assigned to each image.

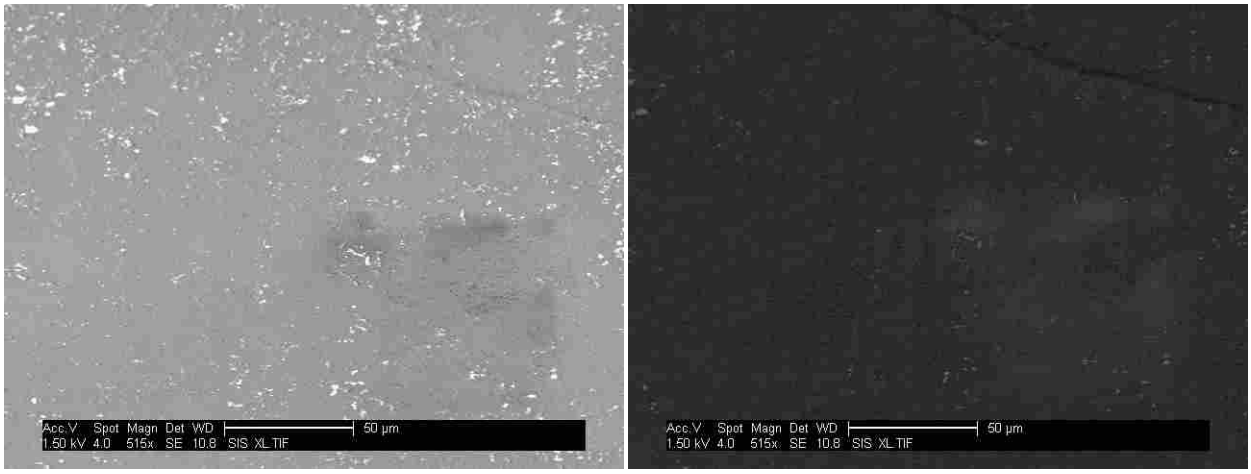

Figure 4 - Representative images from the statistical analysis.

The results were then analyzed by a statistical software package called Minitab (version 15). The following results were obtained:

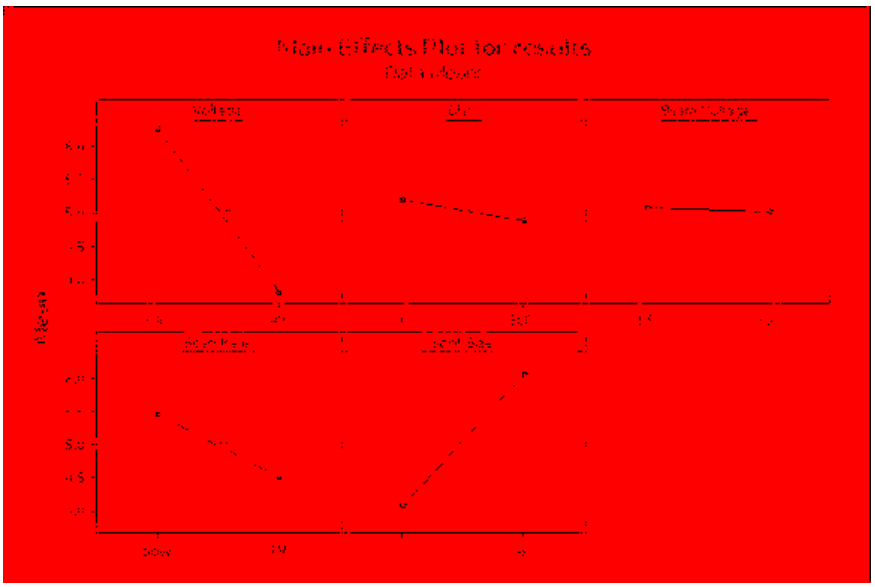

Figure 5 - Main Effects Plot

From the main effects plot (see Figure 5), it is apparent that a better contrast image will be achieved using a negative voltage, slow scan, and a large spot size. Bias and beam voltage had a relatively small effect on contrast quality. Applied voltage has the greatest effect on contrast quality.

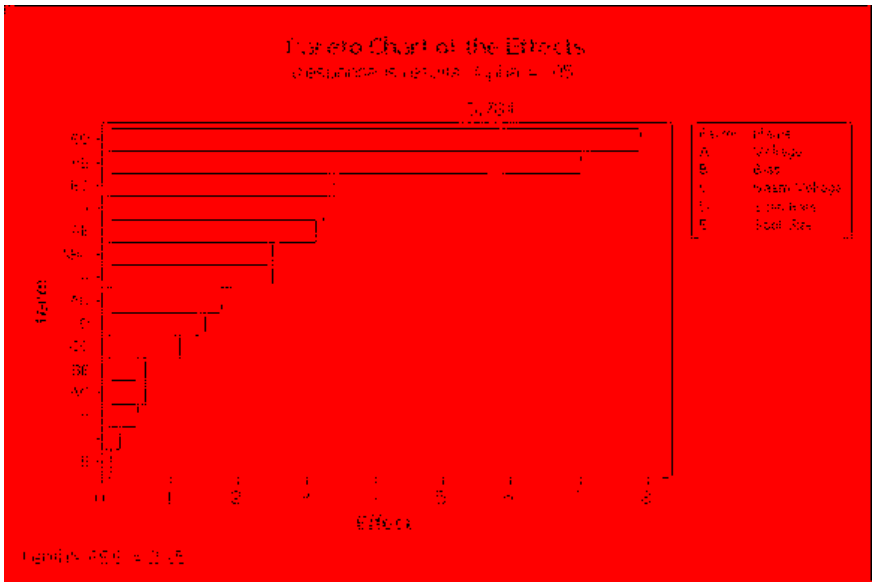

Figure 6 – Pareto Chart of the Effects

From the Pareto chart (see Figure 6) it becomes clear that there are two statistically significant two-factor interactions: Bias/Scan Rate, and Voltage/Spot Size. In order to understand how these factors affect each other, the interaction plot was generated and examined (see Figure 7).

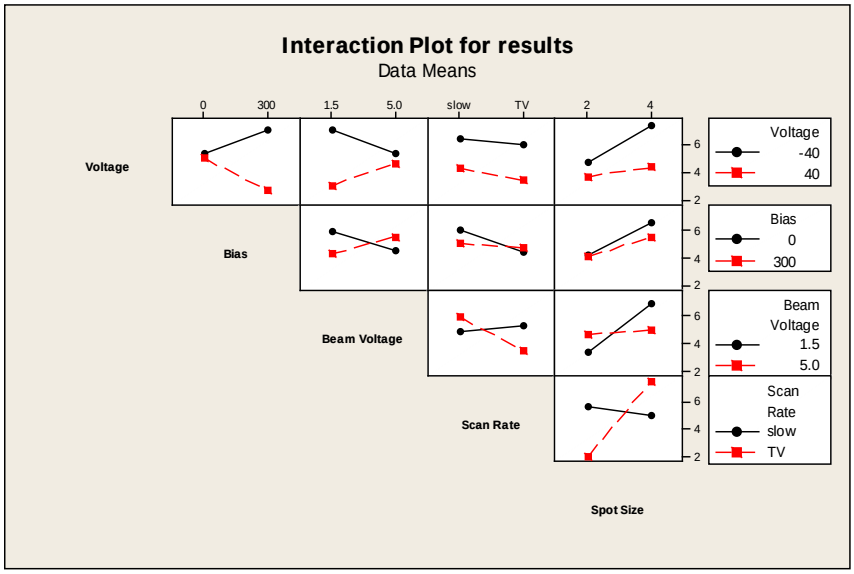

Figure 7 – Interaction Plot for Results

The only plots that are of interest are the two that were identified as statistically significant (bias/scan rate, and voltage/spot size). The voltage/spot size plot (top right) shows that increasing spot size has a stronger effect on improving contrast quality if we use a negative applied voltage. The bias/scan rate plot (center) shows that increasing the scan rate has almost no effect while used with a high bias, but causes a reduced contrast quality when using a high scan rate with a low bias.

To summarize, the statistical analysis shows that the best contrast images are produced using a negative applied voltage and by increasing secondary electron yield by means of slower scan rate and larger spot size. These general guides were used while viewing other nickel filled samples. It was found that when viewing samples for a longer period of time, the quality of contrast was reduced due to charging on the non-conductive areas of the sample. Between statistical results and operator experience, it was shown that the best microscope settings are as follows:

1. Negative applied voltage
2. Low beam voltage
3. Small spot size
4. Fast scan rate
5. Sample tilted toward detector
6. High detector bias

It should be noted that some of the above settings directly contradict the results from the statistical analysis. While the recommended settings work well to create a few contrast images, over time charging builds up, and the contrast is lost. During the statistical analysis, the location on the sample was not held constant because of rampant charging. While that worked well for analyzing the microscope, it is not a practical solution for detecting nano-strand cluster sizes. In general, mitigating charging by reducing the total number of electrons entering the sample serves to maintain better contrast for a greater period of time. This allows better use of the valuable time at the SEM, and was used for all subsequent tests.

2.7 Voltage Contrast on Static Samples

Armed with a solid understanding of voltage contrast, and knowledge of the best settings to use in the SEM, we were finally prepared to obtain preliminary results on nano-strand cluster size. To allow voltage application to the silicone-based nano-composite material, a thin copper wire was inserted into fully cured samples. To improve electrical contact with the conductive reinforcements and to immobilize the wire, silver filled conductive epoxy was applied to the wire and the sample. To ensure adequate insulation from ground, samples were fixed to glass microscope slides, each of which was subsequently fixed to microscope stubs using cyanoacrylate glue (super glue). These samples were not polished due to the elastomeric nature of the silicone matrix.

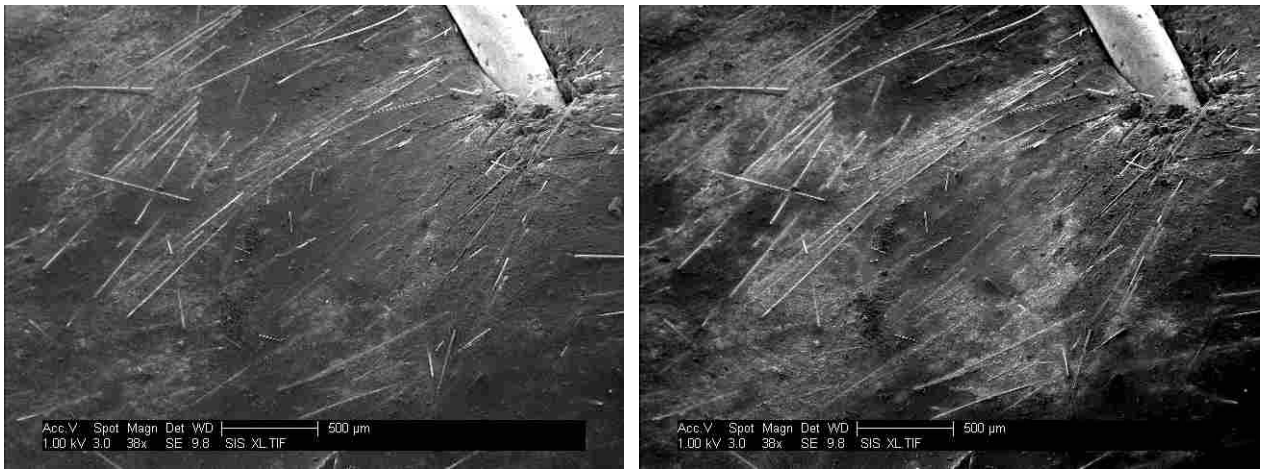

Figure 8 – Voltage contrast of HDSG material. Left = 0VDC, right = -5VDC. Cloudy areas indicate subsurface nano-strand clusters.

Images of the nano-composite show evidence of subsurface nano-strand clusters near the voltage application site. Detailed image analysis is discussed in section 2.9.

2.8 Voltage Contrast of Strained HDSG

In order to observe the change in nano-strand cluster size in response to strain, it becomes necessary to apply strain to the nano-composite while being viewed by the electron microscope. To that end, a specialized tensile stage designed to operate within the SEM vacuum chamber was obtained. The tensile stage requires that the sample be between 17mm and 37mm in length, and 10mm or less in width. A sample meeting these requirements was cut from a sheet of nano-composite material, and an electrical contact was secured using conductive silver filled epoxy. In order to preserve electrical isolation from the grounded tensile stage, balsawood shims were adhered to the ends of the sample, and heatshrink tubing was applied to the copper wire.

Images were taken at 0VDC and -5VDC at multiple locations on the sample at zero strain. The tensile stage was then used to strain the sample 10%, and another series of pictures

was taken across the entire sample (at 0V and -5V). Panoramic pictures were created from the resulting series of images.

Figure 9 – Voltage Contrast panorama of unstrained nano-composite at 0VDC

Figure 10 – Voltage Contrast panorama of unstrained nano-composite at -5VDC

Figure 11 – Voltage Contrast panorama of nano-composite strained to 10% at 0VDC

Figure 12 – Voltage Contrast panorama of nano-composite strained to 10% at -5VDC

2.9 Image Analysis

In the foregoing images, it is easy to see contrast of one area relative to another. A cursory examination of the images however, reveals very little. It is easily inferred that the brighter areas are conducting the negative applied potential, and by extension implies an electrically connected

cluster of nickel nano-strands. In order to quantitatively compare the images, Matlab was used to normalize the area being examined and the initial brightness of the unstrained sample to account for charging and for SEM operator adjustments. After normalizing the images, a brightness threshold was applied so areas could be compared as being black or white, where the white area is presented as a percentage of total image area.

Figure 9: 0V, unstrained, **6.58%**
Figure 10: -5V, unstrained, **28.62%**
Figure 11: 0V, 10% strain, **6.61%**
Figure 12: -5V, 10% strain, **34.16%**

As can be seen, a strain of 10% corresponds to a change in cluster size of approximately 5.5%. When related to the absolute area being measured, 5.5% corresponds to an increase in electrically connected cluster area of 0.98 mm^2.

In order to fuel the percolation model, this new technique is being employed across a broad range of strains for a variety of strain gage compositions. The data from those tests will provide the elusive information required to build an accurate numerical percolation model. The model will then be used to predict properties and performance of future iterations of the synthetically piezoresistive nano-composite. Once created, the accurate model can be used to analyze results from measurements and testing, such as those described in section 3.

3 NANO-COMPOSITE STRAIN GAGE TESTING

3.1 Substrate Motivation

As mentioned earlier, a prime application for synthetically piezoresistive nano-composite material capable of large deformations would be strain sensing. To that end, the nano-composite is being characterized to improve design and tested to demonstrate feasibility. In order to test the nano-composite, strain gages were cut from a sheet of the nano-composite material. Hereafter, the nano-composite strain gages will be referred to as High Displacement Strain Gages (HDSGs). To demonstrate feasibility, biological tissue was chosen as a test substrate inasmuch as biological tissues represent a broad range of materials capable of large strains, the measurement of which is frequently performed by biomechanics researchers.

3.2 Biological Tissue and Large Strain Measurement

Biological tissues are quite unique in that they are capable of facilitating repetitive, dynamic physiological loads. Consider the anterior cruciate ligament (ACL) of the knee, strains up to 12% are experienced during normal physiological motion [16], while the strains in the posterior longitudinal ligament routinely reach 34%[17]. From a research perspective, the strain experienced by a given material is useful measure for quantifying and studying the mechanical behavior and response of a system. Strains of small magnitude (<1%) are easily measured through the use of commercially available strain gages which rigidly fixed to the surface of interest. However, high displacement systems cannot typically be quantified by conventional

strain gages, due to the large strains experienced. As biological tissues have a viscous surface, low stiffness, and frequently experience large strains, the implementation of commercial strain gages is not a viable solution. To overcome this obstacle, researchers will typically use an optical technique such as photoelasticity [18-20], holography [21-23], or elastography [24-26]. The most common approach is an optical method known as Optical Marker Tracking (OMT), which fixes high contrast markers to an area of interest, and then tracks the deformation by simultaneously recording the reaction to the applied loads throughout the deformation [27-30]. The position data can then be extracted from the recording, and used to calculate strain. Unfortunately, this process requires significantly more setup time, specialized equipment, does not provide real-time results, and is sensitive to numerical errors (both in the original position calculation and again in the strain calculation). For these reasons, it is desirable to create strain gages with a higher range of measurable strain.

3.3 HDSG Background

As previously discussed, traditional strain gages fail to measure large displacements. To measure a wider range of strain, a High Displacement Strain Gage (HDSG) must (1) have greater flexibility and (2) experience a measurable change in resistivity throughout its motion. This apparent conflict of requirements can be satisfied through the use of a composite, whose properties can be designed by careful selection of matrix and reinforcement. The nano-composite that was developed for high displacement strain sensing is a synergistic combination of three different materials. The matrix is Dow Corning's® two part silicone elastomer, Sylgard 184. The reinforcement is a combination of nickel nano-strands nickel nano-strands and chopped nickel-coated carbon fiber (NCCF). The nano-strands are manufactured through a proprietary chemical

vapor deposition (CVD) process that creates very high aspect ratios and a highly branched structure (see Figure 13).

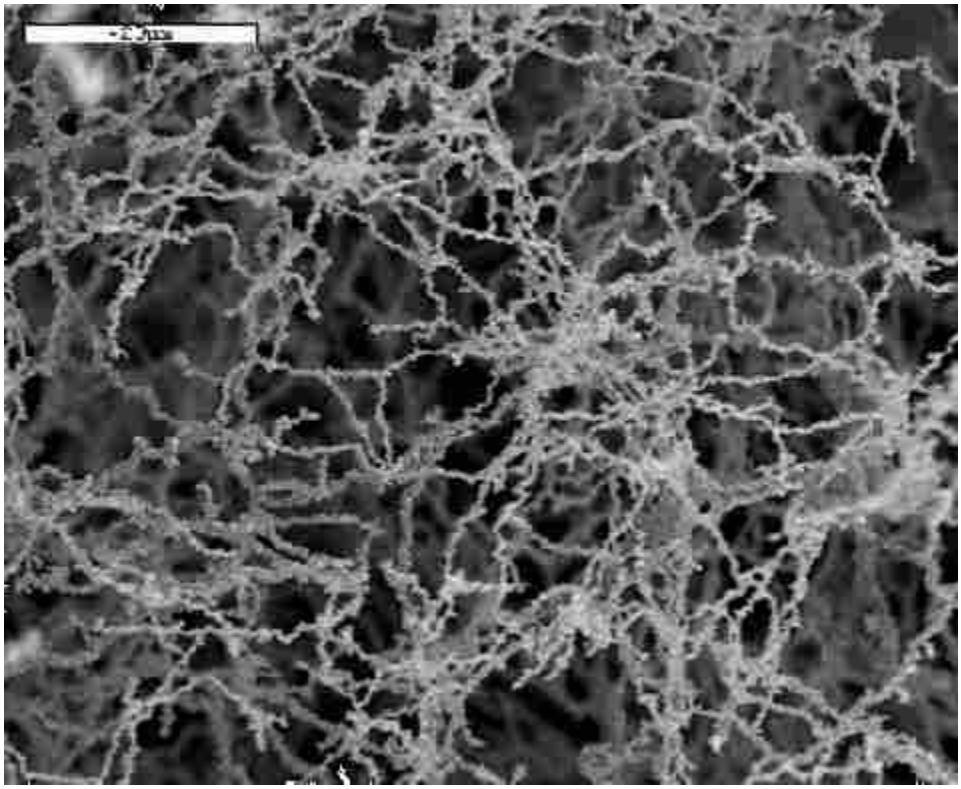

Figure 13 - SEM image of highly branched nickel nano-strands. Image courtesy of Conductive Composites Company.

The chopped nickel-coated carbon fiber is produced by CVD coating nickel onto unsized carbon fiber, and then chopping the coated tow to approximately 2 mm (see Figure 14). The constituent materials are combined using a double planetary mixer, cast into a CNC machined aluminum mold, and cured under vacuum [5].

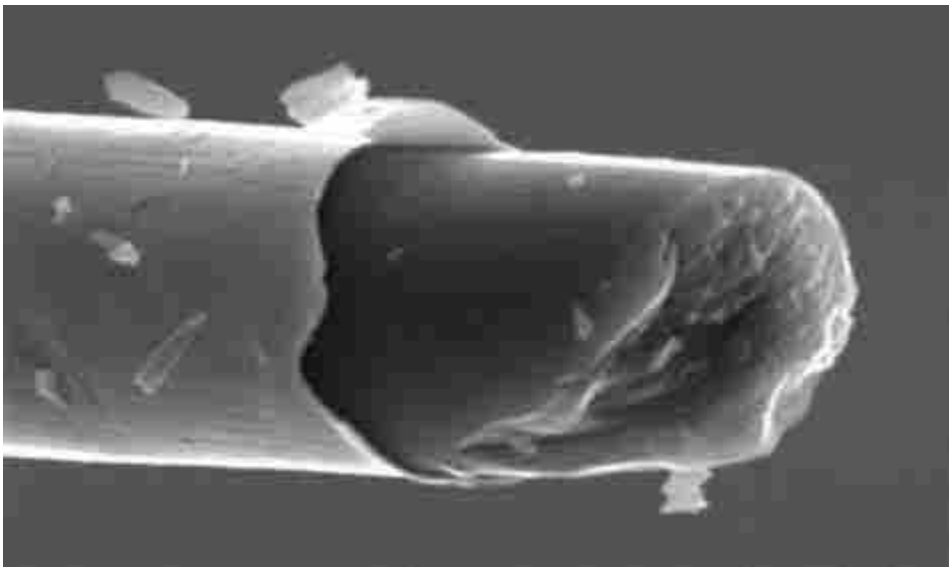

Figure 14 - SEM image of nickel coated carbon fiber (NCCF). Image courtesy of Conductive Composites Company.

3.4 HDSG Properties

As can be expected of any composite, the effective properties are related to the properties of the components. For gage material consisting of 11% nickel nano-strands and 2% NCCF, the effective strain to failure has been measured to be 50% ± 5%, and is limited by the strain to failure properties of the matrix. The electrical properties are more difficult to quantify. While none of the constituents of the nano-composite are naturally piezoresistive, the composite behaves like a piezoresistive material with a negative gage factor. That is to say, in response to an applied load, the resistance goes down. One explanation for this behavior would be to say that the conductive nickel filaments and NCCF progressively come into stronger electrical contact with each other as the HDSG is strained. Naturally, the improved electrical contact would enhance the electrical conductivity, which would correspond to a reduction in resistance.

While it may be convenient to think of the electrical interaction as simple contact between conductors, the insulating silicone matrix fully wets all the reinforcement prior to curing, which

prevents all classical electrical contact. The effect that governs the change in resistance is referred to as “quantum tunneling” (see section 2.2 for discussion). In short, the wave properties of the conduction electrons allow them to jump through or “teleport” past the thin potential energy barrier posed by the insulating matrix where the reinforcements are close to each other [31-33]. The maximum distance that the electrons can jump is related to the electrical properties of silicone, and proportional to the applied voltage. When the HDSG is unstrained, there are an equilibrium number of locations (or junctions) where quantum tunneling can take place. As the HDSG is strained, additional junctions are activated, thus reducing the overall resistance. This change in resistance is measured using a simple circuit known as a voltage divider. The HDSG is placed in series with a known resistor and an applied DC voltage. The voltage drop across the known resistor is measured with a voltmeter, and the change in resistance within the HDSG is then calculated at each point in time:

$$\Delta R_{HDSG}=\frac{R_1 * V_S}{V_{Drop}} - R_1 \tag{1}$$

Where R_1 is the resistance of the known resistor, V_S is the voltage of the source, and V_{Drop} is the measured voltage drop across the known resistor. The overall conductivity depends on the number of junctions that are activated during a deformation, meaning the change of magnitude in conductivity depends on the geometry of the particular gage being considered. This measured result is normalized by solving for resistivity, ρ:

$$\rho=R*\frac{A}{l} \tag{2}$$

Where R is the resistance as a function of strain, A is the cross sectional area, and *l* is the length.

Another important property of strain gages is the “gage factor”. The gage factor (or strain factor) is the ratio of relative change in electrical resistance to the mechanical strain ε. That is to say,

$$GF = \frac{\Delta R}{R_0 * \varepsilon} \tag{3}$$

Large gage factors are desirable as they allow for higher resolution measurement per unit strain. The magnitude of the gage factor of the HDSGs tested was found to be above 5, whereas commercially available metallic strain gages have a typical value of about 2.

3.5 Testing

The HDSGs were tested to validate the usability of the HDSG in biological applications, and assess their ability to measure a repeated strain accurately. Sectioned bovine Achilles tendons were used as the test substrate onto which the HDSG and optical markers were attached (see Figure 15).

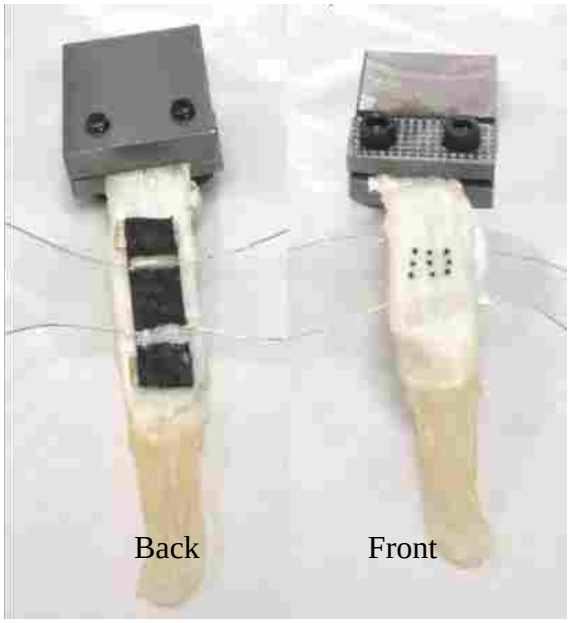

Figure 15 - Sectioned bovine ligament in test fixture with HDSG (left) and optical markers (right)

Cyanoacrylate glue (super glue) was used as the adhesive. In order to overcome the non-bonding characteristics of cured silicone, a hand-held tesla coil was used to oxidize the glue surfaces of the HDSG. Contrary to standard strain gage attachment, the HDSG was only attached at the ends, in order to prevent modification of the tendon properties. Additionally, the HDSG needed to maintain electrical isolation from the ligament, because ligaments are both conductive and slightly piezoelectric. The conductivity of the ligament would effectively short out the voltage divider, and the piezoelectricity would cause a false reading on the voltage drop in the circuit. Lead shot was used for the optical markers, as they are small, reasonably consistent in size, and provide high contrast with the light background of the ligament. The optical markers were attached using a gel formulation of cyanoacrylate glue, in a 3x3 matrix pattern (see Figure 15).

The changing resistance of the HDSG at each time step was measured with a voltage divider which was automatically recorded by a Data Acquisition system (DAQ). The positions of the optical markers were recorded by two orthogonal cameras equidistant from the sample, which were calibrated just prior to testing the prepared ligaments. The video feed from the cameras was also recorded by the DAQ using the same time interval as the voltage readings (10 Hz). The tendon was pulled in a load frame with a force of 50 pounds, which force was applied five times in a sine wave cycled at 1/20 Hz. The resulting resistance was recorded in a spreadsheet along with the force and displacement output by the load cell and crosshead respectively.

3.6 Data Analysis

The information measured directly from the straining tendon is not strain, but is sufficient to determine strain. For the optical marker tracking, the direct measurement was thousands of sequenced jpeg images. The images were processed in Matlab using Digital Linear Transformation to determine the x, y, and z position in space of each optical marker at each time step. The position data can then be used to calculate strain by drawing line segments interconnecting four mutually adjacent optical markers. Assuming the markers to exist in three dimensions, six line segments will be required to connect all four markers to each other, resulting in a tetrahedron. This same tetrahedron can be redrawn at a subsequent time step, and the following equation can be applied to calculate the full strain tensor:

$$\begin{Bmatrix} \left(\Delta s^2 - \Delta s_0^2\right)_1 \\ \left(\Delta s^2 - \Delta s_0^2\right)_2 \\ \left(\Delta s^2 - \Delta s_0^2\right)_3 \\ \left(\Delta s^2 - \Delta s_0^2\right)_4 \\ \left(\Delta s^2 - \Delta s_0^2\right)_5 \\ \left(\Delta s^2 - \Delta s_0^2\right)_6 \end{Bmatrix} = \begin{bmatrix} \left(2\Delta X_1^2\right)_1 & \left(2\Delta X_2^2\right)_1 & \left(2\Delta X_3^2\right)_1 & \left(4\Delta X_1\Delta X_2\right)_1 & \left(4\Delta X_2\Delta X_3\right)_1 & \left(4\Delta X_1\Delta X_3\right)_1 \\ \left(2\Delta X_1^2\right)_2 & \left(2\Delta X_2^2\right)_2 & \left(2\Delta X_3^2\right)_2 & \left(4\Delta X_1\Delta X_2\right)_2 & \left(4\Delta X_2\Delta X_3\right)_2 & \left(4\Delta X_1\Delta X_3\right)_2 \\ \left(2\Delta X_1^2\right)_3 & \left(2\Delta X_2^2\right)_3 & \left(2\Delta X_3^2\right)_3 & \left(4\Delta X_1\Delta X_2\right)_3 & \left(4\Delta X_2\Delta X_3\right)_3 & \left(4\Delta X_1\Delta X_3\right)_3 \\ \left(2\Delta X_1^2\right)_4 & \left(2\Delta X_2^2\right)_4 & \left(2\Delta X_3^2\right)_4 & \left(4\Delta X_1\Delta X_2\right)_4 & \left(4\Delta X_2\Delta X_3\right)_4 & \left(4\Delta X_1\Delta X_3\right)_4 \\ \left(2\Delta X_1^2\right)_5 & \left(2\Delta X_2^2\right)_5 & \left(2\Delta X_3^2\right)_5 & \left(4\Delta X_1\Delta X_2\right)_5 & \left(4\Delta X_2\Delta X_3\right)_5 & \left(4\Delta X_1\Delta X_3\right)_5 \\ \left(2\Delta X_1^2\right)_6 & \left(2\Delta X_2^2\right)_6 & \left(2\Delta X_3^2\right)_6 & \left(4\Delta X_1\Delta X_2\right)_6 & \left(4\Delta X_2\Delta X_3\right)_6 & \left(4\Delta X_1\Delta X_3\right)_6 \end{bmatrix} \begin{Bmatrix} E_{11} \\ E_{22} \\ E_{33} \\ E_{12} \\ E_{23} \\ E_{13} \end{Bmatrix}$$

Where Δs is the length of a given line segment at time step N, Δs_0 is the change in length of a given line segment between time step zero and N, ΔX_1 is the difference in x position for the two end points of a line, ΔX_2 is the difference in y position for the two end points of a line, and ΔX_3 is the difference in z position for the two end points of a line. We recognize this matrix equation to be of the form A = B*C. Solving for C, we find that $C = B^{-1}*A$. This equation must be solved for each of four tetrahedrons formed by the nine optical markers at each time step. Matlab code was developed to complete this operation, but due to the highly planar geometry of the imaginary

tetrahedrons, many of the inverted B matrices encountered singularities, and failed to provide strain data. To ameliorate this issue, strain was calculated according to the equation:

$$\varepsilon = \frac{\Delta L}{L_0} \tag{4}$$

Where ΔL is the change in distance between two rows of optical markers between time step zero and N, and L_0 is the initial distance between two rows of optical markers. It is recognized that soft tissue strain is frequently calculated as a full tensor, but the one dimensional case is considered sufficient here as the HDSGs are currently limited to sensing strain in one dimension only.

As for the strain gage data, the direct measurement was the voltage drop across the HDSG at each time step. As the HDSG was strained with the tendon, the resistance became small, and the voltage drop also became small. Change in resistivity was calculated at each time step according to equations (1) and (2). Considering the electrical nature of the composite material, it was not surprising to see that the magnitude of the resistivity significantly varied from test to test (nearly a factor of two). To compensate for this, the resistivity was normalized by the equation:

$$\rho = \frac{\rho_t}{\rho_0} \tag{5}$$

Where ρ_t is the value of resistivity at time step *t*, and ρ_0 is the resistivity at time step zero.

As with any strain gage, the changing resistance is meaningless without a calibration. Thus, the true strain as measured by the optical markers on the first test was used to calibrate the resistivity data from the HDSG on the first test. We expect resistivity to vary exponentially with strain (see section 2.2), and therefore calibrated the data using a target exponential of the form:

$$A = Be^{Ct} - D \tag{6}$$

The fit was performed using Matlab's 'fminsearch' function, where A, B, C and D were found to be 1.9998, -2.8269, 0.0281, and -1.8395 respectively. This calibration was then applied to the resistivity data from the other tests, resulting in strain data.

3.7 Results

Having calculated strain using two independent measuring techniques, we can compare the resulting values to determine the validity of the new HDSG technique. The calibrated strain data is compared with the true strain as measured by the optical markers in the figures below. When superimposed, it is easily observed that the HDSG reasonably approximates the true strain despite some error. The average error for all the tests was calculated to be 7.1% (see Figure 16, Figure 17, and Figure 18).

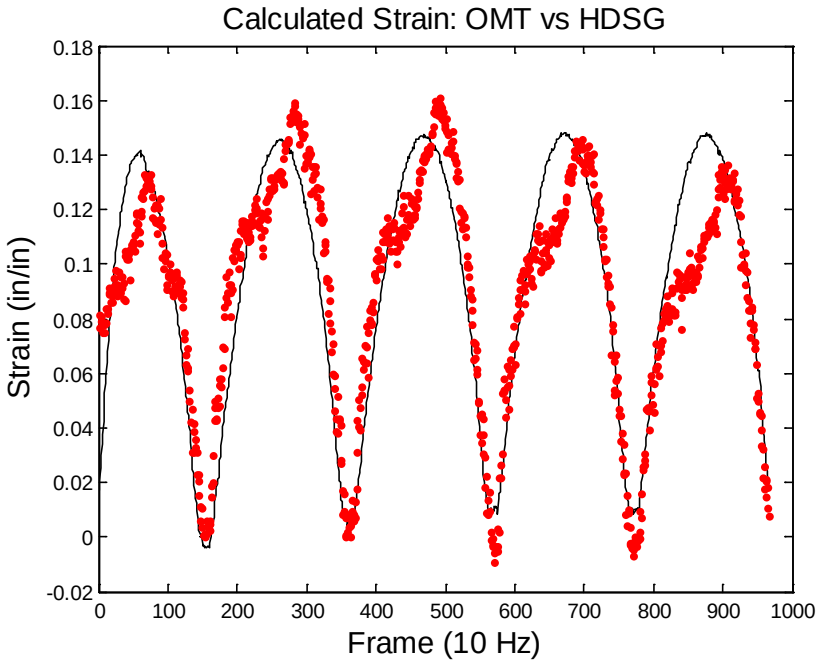

Figure 16 – Test 1: Calibration used to compare resistivity with strain. True strain (as measured by OMT) is the smooth black line, and strain as measured by the HDSG is show as red data points (error = 5.5%)

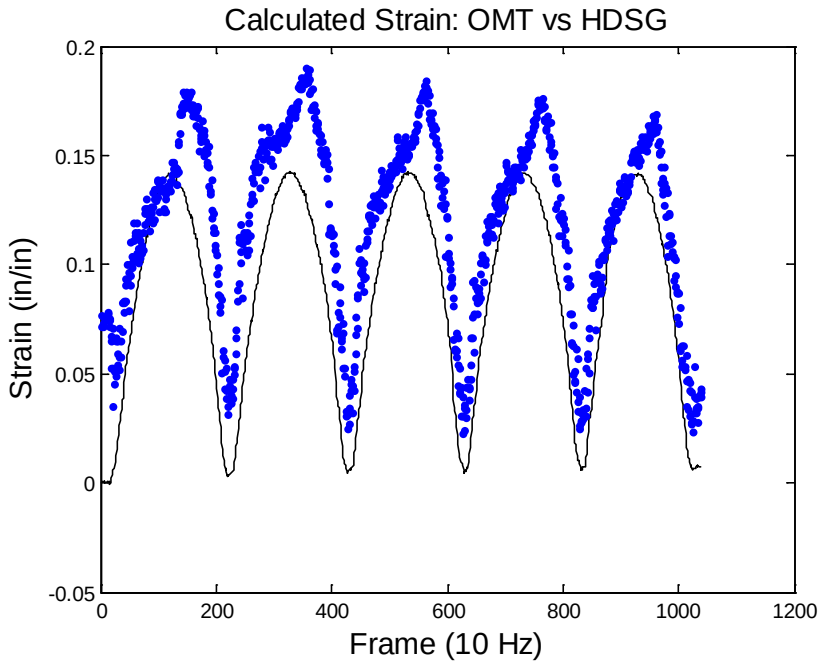

Figure 17 – Test 2: Strain as measured by optical marker tracking vs. HDSG resistivity. True strain (as measured by OMT) is the smooth black line, and strain as measured by the HDSG is show as blue data points (error = 8.9%)

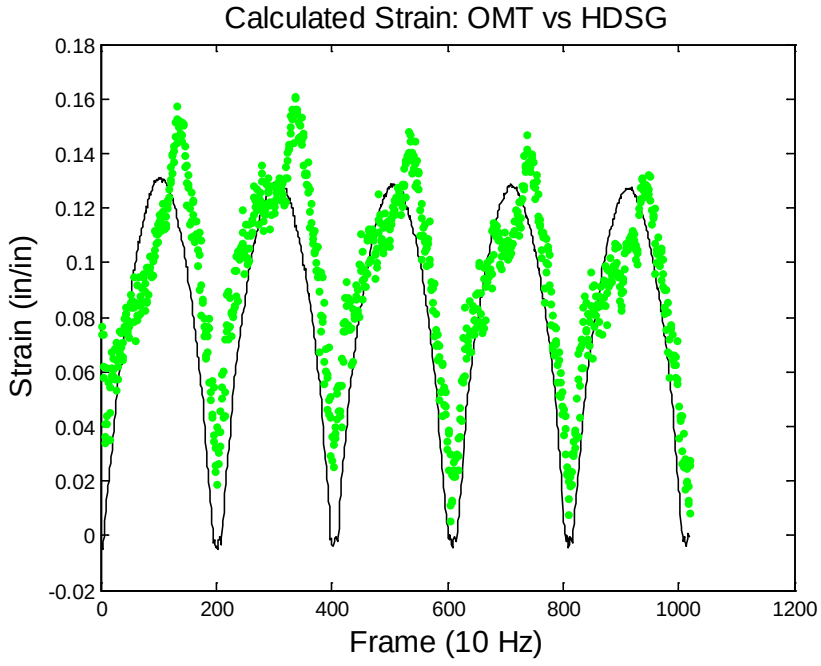

Figure 18 – Test 3: Strain as measured by optical marker tracking vs. HDSG resistivity. True strain (as measured by OMT) is the smooth black line, and strain as measured by the HDSG is show as green data points (error = 6.9%)

While the error is acceptably low, it is observed that the majority of the error is concentrated near the crest of each cycle. Specifically, just left of each peak there is a grouping of data points that does not continue to follow the expected path. The grouping indicates a period during which voltage drop across the HDSG does not change significantly, even though the strain is continuing to change. This behavior is unexpected, but could be the result of relaxation modulus, fiber pull-out, entanglement, or any combination thereof. Each of these will be discussed briefly here.

Relaxation Modulus

As previously mentioned, the tendon was loaded up to 50 lbs following a sine wave. In following that curve, the rate of change of force application changes significantly near the peaks and troughs. By changing the rate of force application, the strain rate will have also changed. The Poisson thinning of the silicone at the quantum tunneling junctions has been assumed to be linear with strain, but the relationship with strain *rate* has not been examined. It is possible that the relaxation modulus of the material is causing non-linearities, leading to the unexpected electrical behavior.

Fiber Pull-out

The discontinuous nickel coated carbon fibers are significantly thicker and stiffer than the nickel nano-strands, and are therefore less easily influenced by the straining silicone matrix. It is possible that after reaching a certain level of strain, the shear forces at the interface between the carbon fibers and the silicone matrix overcomes the friction holding them together, allowing the carbon fiber to ‘pull-out’. The strain is not so high, however, so as to allow macroscopic nano-composite failure. Thus, when the strain begins to drop, the carbon fiber is allowed to slide back into the shaft that it left behind when it pulled out. If this is the case, the motion of the carbon

fibers may cause some quantum tunneling junctions to deactivate temporarily. The unexpected deactivation of these junctions could explain the peculiar electrical behavior.

Entanglement

The nickel nano-strands exhibit a highly branched and interconnected structure (see figure 13). While the nickel is very stiff relative to the silicone matrix, the nano-strands' relative position will change when the matrix is strained. After a certain amount of strain however, the nickel will begin to impede further nickel motion, similar to the way a tangled wad of fishing line behaves. It can stretch easily a certain amount, but then the entanglement begins to affect the force required per unit deformation. If there were a sudden change in the relative stiffness of the material, the rate at which quantum tunneling junctions are activated would be affected, causing a change in the electrical response.

Several tests have been proposed to test these hypotheses. For example, to determine if the relaxation modulus is the source of error, one would conduct the same set of experiments except using a triangle wave or a sine wave of different frequency. If the grouping remains unaffected, then the error is clearly not due to relaxation modulus. Alternately one might conduct the same experiment with a different target strain level. If the grouping occurs just below the peak regardless of the applied strain, the error is not the result of fiber pull-out. Perhaps the most useful set of experiments however, will be those described in section 2.9 – once a valid numerical model has been created, the model can be used to predict electrical behavior. If the grouping can be predicted with the model, the model can also be used to predict how to prevent grouping.

3.8 HDSG Conclusions

The HDSG material being investigated is a viable option for measuring large strains in one direction. While the technology has room for improvement, it has been shown to provide accurate results measuring strain in one dimension without the expense, equipment, tedium and numerical singularities introduced by resorting to conventional OMT methods. The HDSG technique has application to most biological tissue characterization applications. This could include anything from strain monitoring on the skin of an athlete recovering from a muscle injury, all the way to research of spinal ligament characterization. This technique also has strong prospects in many other fields such as Human Machine Interface (HMI) applications; including touch-screens or position and motion sensors. Further work should be done to investigate HDSG performance over time and methods for reducing error. One way to improve HDSG performance will be to optimize the relative concentration of conductive reinforcements. When the "recipe" has been optimized, there will be a near-linear change in resistance throughout a large deformation. In order to optimize the relative concentrations of conductive reinforcements, a statistical design of experiments (DOE) has been proposed, and will be conducted in the near future.

4 CONCLUSIONS AND FUTURE WORK

The main goal of this research has been to advance the state of the art for solid state wide range strain sensing. A major barrier to predicting behavior is the inaccuracy of the prevailing model, which uses percolation theory. To improve the model, efforts have been concentrated toward quantifying the size of electrically connected nickel nano-strand clusters within the nano-composite. A novel application of an SEM technique has been developed and employed which allows the visualization of electrically connected areas, and progress is being made toward average cluster size prediction.

In addition to advancing the theoretical aspects of the technology, experimental validation has been performed to prove the feasibility of the nano-composite as a sensor. The material was tested was on bovine Achilles tendon, as it is bio-mechanical soft tissue which is representative of many applications where a solid state strain sensor would be invaluable. Results demonstrated that the HDSGs can measure strain with greater than 90% accuracy, and also illuminated areas requiring further development and testing.

Future work will include improvements in characterization and experimental validation. Characterization should implement the SEM technique to observe nano-strand cluster size in samples with varying nickel content across a range of applied strains, and results will be used to create a valid and useful percolation model. The relative concentration of conductive reinforcements should be optimized. After the valid percolation model has been created, the model can be used to compare with and validate the tests described in section 3.7. Testing

should include HDSG strain measurement on other substrates such as deforming structures or Human Machine Interfaces. Additionally, HDSGs should be investigated as a way to study strain in two dimensions simultaneously. This could be accomplished using a HDSG in the shape of a square or cross with an AC signal.

The significance of these findings can be seen in a variety of spheres of influence. Within the field of research, the newfound ability to sense nano-strands connected by quantum tunneling junctions has opened the door to experimental model validation. Additionally, having demonstrated actual measurement of strain, many more applications are sure to follow. Within the global science community, these results will surely fuel research in similar areas. Within the commercial sector, the market for large strain sensing (which has been dominated by optical methods for decades) will surely receive stiff competition from these or similar nano-composite sensors in the coming years. While this marks the end of this thesis, the nano-composite sensor story is far from over.

REFERENCES

1. Window, A.L., *Strain Sensor Technology*. 1992, London and New York: Elsevier Applied Science.
2. Bokobza, Liliane. "Multiwall Carbon Nanotube Elastomeric Composites: A Review." *Polymer* 48 (2007): 4907-4920.
3. Zhou, J.F., Y.H. Song, Q. Zheng, Q. Wu, and M.Q. Zhang. "Percolation Transition and Hydrostatic Piezoresistance for Carbon Black Filled Poly(Methylvinylsilioxane) Vulcanizates." *Carbon* 46 (2008): 679-691.
4. Yamaguchi, K., J. J. C. Busfield, and A. G. Thomas. "Electrical and Mechanical Behavior of Filled Elastomers. I. The Effect of Strain." *Journal of Polymer Science Part B: Polymer Physics* 41, no. 17 (2003): 2079-2089.
5. Johnson, Oliver K., George C. Kaschner, Thomas A. Mason, David T. Fullwood, Tommy Hyatt, Brent L. Adams, and George Hansen. "Extreme Piezoresistivity of Silicone/Nickel Nanocomposite for High Resolution Large Strain Measurement." In *TMS 2010*. Seattle, 2010.
6. Stokes, H.T., *Solid State Physics for Advanced Undergraduate Students*. 4 ed. 2007, Provo: BYU Academic Publishing. 70.
7. Grimmett, G., *Percolation. 2nd ed.* A series of comprehensive studies in mathematics. Vol. 321. 1999: Springer.
8. Sahimi, Muhammad. "Critical Exponent of Percolation Conductivity by Finite-Size Scaling." *Journal of Physics C: Solid State Physics* 16 (1983): L521-527.
9. Leinonen, Kari. "Investigation of Voltages and Electric Fields in Silicon Radiation Detectors Using a Scanning Electron Microscope." *Nuclear Instruments & Methods in Physics Research* (2005): 411-419.
10. Dale E. Newbury, D.C.J., Patrick Echlin, Charles E Fiori, Joseph I. Goldstein, *Advanced scanning electron microscopy and X-ray microanalysis*. illustrated ed. 1986. 454.
11. Wells, O.C., *Scanning Electron Microscopy*. 1974: McGraw-Hill.
12. CMI, "Scanning Electron Microscope (Sem) Machine Variables", Center for Microscopy and Imaging (CMI) at Smith College http://131.229.114.77/microscopy/semvar.html (accessed 23 May 2010 2010).
13. Z. Gemmill, L. Durbha, S. Jacobson, G. Gao, K. Weaver. "Sem and Fib Passive Voltage Contrast." In *Microelectronics Failure Analysis: Desk Reference*, 2004.
14. Gatan, "An Introduction to Ebic" http://www.gatan.com/files/PDF/products/Introduction_to_EBIC.pdf.
15. Parish, Chad. "Tutorial: Electron Beam-Induced Current in the Scanning Electron Microscope." *Microscopy and Analysis* Sept 2007 (2007).

16. Bach, J. M., M. L. Hull, and H. A. Patterson. "Direct Measurement of Strain in the Posterolateral Bundle of the Anterior Cruciate Ligament." *J Biomech* 30, no. 3 (1997): 281-3.
17. Chazal, J., A. Tanguy, M. Bourges, G. Gaurel, G. Escande, M. Guillot, and G. Vanneuville. "Biomechanical Properties of Spinal Ligaments and a Histological Study of the Supraspinal Ligament in Traction." *J Biomech* 18, no. 3 (1985): 167-76.
18. Nienhaus, U., T. Aegerter-Wilmsen, and C. M. Aegerter. "Determination of Mechanical Stress Distribution in Drosophila Wing Discs Using Photoelasticity." *Mech Dev* (2009).
19. Heller, W., and H. Oppenheimer. "Comparative Studies on Photoelasticity of Elastomers and Plastomers." *J Colloid Sci* 3, no. 1 (1948): 33-43.
20. Ainola, L., and H. Aben. "Fringe Patterns in Integrated Photoelasticity." *J Opt Soc Am A Opt Image Sci Vis* 26, no. 7 (2009): 1714-20.
21. Rosso, V., R. Beland, S. Lecler, Y. Renotte, S. Habraken, Y. Lion, and P. Charette. "Simultaneous Strain and Coherent Imaging Using Coupled Photorefractive Holography and Shearography through Scattering Media." *J Biomed Opt* 13, no. 4 (2008): 044010.
22. Matsumoto, T., T. Watanabe, and A. Kojima. "Deformation Analysis of the Human Femur by Holographic Interferometry." *Conf Proc IEEE Eng Med Biol Soc* 2007 (2007): 4699-701.
23. De la Torre-Ibarra, M., F. Mendoza-Santoyo, C. Perez-Lopez, and S. A. Tonatiuh. "Detection of Surface Strain by Three-Dimensional Digital Holography." *Appl Opt* 44, no. 1 (2005): 27-31.
24. Chen, L., G. M. Treece, J. E. Lindop, A. H. Gee, and R. W. Prager. "A Quality-Guided Displacement Tracking Algorithm for Ultrasonic Elasticity Imaging." *Med Image Anal* 13, no. 2 (2009): 286-96.
25. Rao, M., and T. Varghese. "Correlation Analysis of Three-Dimensional Strain Imaging Using Ultrasound Two-Dimensional Array Transducers." *J Acoust Soc Am* 124, no. 3 (2008): 1858-65.
26. Tsubai, M., O. Fukuda, N. Ueno, T. Horie, and S. Muraki. "Development of an Ultrasound System for Measuring Tissue Strain of Lymphedema." *Conf Proc IEEE Eng Med Biol Soc* 2008 (2008): 5294-7.
27. Sato, K., T. Adachi, D. Ueda, M. Hojo, and Y. Tomita. "Measurement of Local Strain on Cell Membrane at Initiation Point of Calcium Signaling Response to Applied Mechanical Stimulus in Osteoblastic Cells." *J Biomech* 40, no. 6 (2007): 1246-55.
28. Nicolella, D. P., A. E. Nicholls, J. Lankford, and D. T. Davy. "Machine Vision Photogrammetry: A Technique for Measurement of Microstructural Strain in Cortical Bone." *J Biomech* 34, no. 1 (2001): 135-9.
29. McCulloch, A. D., and J. H. Omens. "Non-Homogeneous Analysis of Three-Dimensional Transmural Finite Deformation in Canine Ventricular Myocardium." *J Biomech* 24, no. 7 (1991): 539-48.
30. Lujan, T. J., S. P. Lake, T. A. Plaizier, B. J. Ellis, and J. A. Weiss. "Simultaneous Measurement of Three-Dimensional Joint Kinematics and Ligament Strains with Optical Methods." *J Biomech Eng* 127, no. 1 (2005): 193-7.
31. Bloor, D., A. Graham, E. J. Williams, P. J. Laughlin, and D. Lussey. "Metal-Polymer Composite with Nanostructured Filler Particles and Amplified Physical Properties." *Appl Phys Lett* 88 (2006): 102-103.

32. *Peratech Limited:* *http://www.peratech.com/*. Quantum Tunneling Composites]. Available from: http://www.peratech.com/.
33. Palmer, Jason. "Quantum Trick for Pressure-Sensitive Mobile Devices." *BBC News* (9 Feb 2010). http://news.bbc.co.uk/2/hi/science/nature/8504373.stm.

APPENDIX

Matlab Code – 3D Strain Tensor Calculation

```
%TENSOR Calculations
clear all;
clc;

% To Easily change settings, change test
test = 1;

X=1;
Y=2;
Z=3;

if(test)
    numOBoxes = 1;
    numOPoints = 4;
    startCol = 2;
    numToAvg = 1;
    file = 'test.xls';
    sheet = 'sheet1';
else
    numOBoxes = 4;
    numOPoints = 9;
    startCol = 8;
    numToAvg = 10;
    file = 'lig2.xls';
    sheet = 'lig2a';
end

disp(strcat('Reading from ''',file,''' and sheet ''',sheet,''''));
%read data from spreadsheet
datamat = xlsread(file, sheet);

% Tenmat represents the 6x6 Coefficents matrix
tenmat = zeros(6,6,numOBoxes);

% Begin calculating components of the 3D tensor equation
count = 0;
for i=startCol:3:startCol+(numOPoints-1)*3
    %determine the average x,y,z start position for all 9 points
    count = count +1;
    x(count) = sum(datamat(1:numToAvg,i))/numToAvg;
    y(count) = sum(datamat(1:numToAvg,i+1))/numToAvg;
    z(count) = sum(datamat(1:numToAvg,i+2))/numToAvg;

end

%               Rows of Data, xyz, Point#
pts = zeros(length(datamat)-numToAvg,3,numOPoints);
```

```
      for i = 1:numOPoints
          pts(:,:,i)     =     datamat(numToAvg+1:length(datamat),startCol+(i-
1)*3:startCol+(i-1)*3+2);
      end

      deltax = zeros(numOBoxes,6);
      deltay = zeros(numOBoxes,6);
      deltaz = zeros(numOBoxes,6);
      for box = 1:numOBoxes
          %defines  the  top  left  corner  of  each  of  the  4  squares  being
considered
          %this allows me to define the four dots in each box as 1,2,3 and 4,
          %where 1 is the top left corner, 2 is top right, 3 is bottom left,
          %and 4 is bottom right

          if(numOBoxes == 4)
              if box == 1
                  corner = 1;
              elseif box == 2
                  corner = 2;
              elseif box == 3
                  corner = 4;
              elseif box == 4
                  corner = 5;
              end
              c(1) = corner;
              c(2) = corner + 1;
              c(3) = corner + 3;
              c(4) = corner + 4;
          end
          if(numOBoxes == 1)
              c(1) = 1;
              c(2) = 2;
              c(3) = 3;
              c(4) = 4;
          end

          % 1  2  3
          %
          % 4  5  6
          %
          % 7  8  9

          for j=1:6
              if j == 1 %line one connects dot 1 and 2
                  deltax(box,j) = (x(c(1)) - x(c(2)));
                  deltay(box,j) = (y(c(1)) - y(c(2)));
                  deltaz(box,j) = (z(c(1)) - z(c(2)));


              elseif j == 2 %line 2 connects dot 2 and 3
                  deltax(box,j) = (x(c(2)) - x(c(3)));
                  deltay(box,j) = (y(c(2)) - y(c(3)));
                  deltaz(box,j) = (z(c(2)) - z(c(3)));

              elseif j == 3 %line 3 connects dot 3 and 4
                  deltax(box,j) = (x(c(3)) - x(c(4)));
```

```
                deltay(box,j) = (y(c(3)) - y(c(4)));
                deltaz(box,j) = (z(c(3)) - z(c(4)));

            elseif j == 4 %line 4 connects dot 4 and 1
                deltax(box,j) = (x(c(4)) - x(c(1)));
                deltay(box,j) = (y(c(4)) - y(c(1)));
                deltaz(box,j) = (z(c(4)) - z(c(1)));

            elseif j == 5 %line 5 connects dot 1 and 3
                deltax(box,j) = (x(c(1)) - x(c(3)));
                deltay(box,j) = (y(c(1)) - y(c(3)));
                deltaz(box,j) = (z(c(1)) - z(c(3)));

            elseif j == 6 %line 6 connects dot 2 and 4
                deltax(box,j) = (x(c(2)) - x(c(4)));
                deltay(box,j) = (y(c(2)) - y(c(4)));
                deltaz(box,j) = (z(c(2)) - z(c(4)));
            end

            %solve for the 6x6 matrix that depends on the initial positions
            %(four  boxes  in  the  3x3  array  of  markers,  therefore  4
matricies)

            tenmat(j,1,box) = 2*(deltax(box,j)^2);
            tenmat(j,2,box) = 2*(deltay(box,j)^2);
            tenmat(j,3,box) = 2*(deltaz(box,j)^2);
            tenmat(j,4,box) = 4*deltax(box,j)*deltay(box,j);
            tenmat(j,5,box) = 4*deltay(box,j)*deltaz(box,j);
            tenmat(j,6,box) = 4*deltax(box,j)*deltaz(box,j);
        end
    end

    for i = 1:length(pts)
        for box = 1:numOBoxes
            %determine which point is the top-left corner
            if(numOBoxes == 4)
                if box == 1
                    corner = 1;
                elseif box == 2
                    corner = 2;
                elseif box == 3
                    corner = 4;
                elseif box == 4
                    corner = 5;
                end
                c(1) = corner;
                c(2) = corner + 1;
                c(3) = corner + 3;
                c(4) = corner + 4;
            end
            if(numOBoxes == 1)
                c(1) = 1;
                c(2) = 2;
                c(3) = 3;
                c(4) = 4;
            end
```

```
            for j = 1:6

                %     1 - L1 - 2
                %     | \   /  |
                %     L5  X   L6
                %     | L2  L4 |
                %     3 - L3 - 4

                if j == 1 %line one connects dot 1 and 2

                    defx = abs( pts(i, X, c(1)) - pts(i, X, c(2)) );
                    defy = abs( pts(i, Y, c(1)) - pts(i, Y, c(2)) );
                    defz = abs( pts(i, Z, c(1)) - pts(i, Z, c(2)) );

                elseif j == 2 %line 2 connects dot 2 and 3
                    defx = abs( pts(i, X, c(2)) - pts(i, X, c(3)) );
                    defy = abs( pts(i, Y, c(2)) - pts(i, Y, c(3)) );
                    defz = abs( pts(i, Z, c(2)) - pts(i, Z, c(3)) );

                elseif j == 3 %line 3 connects dot 3 and 4

                    defx = abs( pts(i, X, c(3)) - pts(i, X, c(4)) );
                    defy = abs( pts(i, Y, c(3)) - pts(i, Y, c(4)) );
                    defz = abs( pts(i, Z, c(3)) - pts(i, Z, c(4)) );

                elseif j == 4 %line 4 connects dot 4 and 1

                    defx = abs( pts(i, X, c(4)) - pts(i, X, c(1)) );
                    defy = abs( pts(i, Y, c(4)) - pts(i, Y, c(1)) );
                    defz = abs( pts(i, Z, c(4)) - pts(i, Z, c(1)) );

                elseif j == 5 %line 5 connects dot 1 and 3

                    defx = abs( pts(i, X, c(1)) - pts(i, X, c(3)) );
                    defy = abs( pts(i, Y, c(1)) - pts(i, Y, c(3)) );
                    defz = abs( pts(i, Z, c(1)) - pts(i, Z, c(3)) );

                elseif j == 6 %line 6 connects dot 2 and 4

                    defx = abs( pts(i, X, c(2)) - pts(i, X, c(4)) );
                    defy = abs( pts(i, Y, c(2)) - pts(i, Y, c(4)) );
                    defz = abs( pts(i, Z, c(2)) - pts(i, Z, c(4)) );

                end

                %solve for S^2 terms
                deltaS0squared(j)                                                   =
deltax(box,j)^2+deltay(box,j)^2+deltaz(box,j)^2;
                deltaSsquared(j) = defx^2 + defy^2 + defz^2;

                smat(j) = deltaSsquared(j)-deltaS0squared(j);
            end

      % E is the elements in the strain tensor vector
            E = inv(tenmat(:,:,box))*smat';
            %save the results of E into a matrix
```

```
            tensorstorage(i, 6*(box-1)+1) = E(1);
            tensorstorage(i, 6*(box-1)+2) = E(2);
            tensorstorage(i, 6*(box-1)+3) = E(3);
            tensorstorage(i, 6*(box-1)+4) = E(4);
            tensorstorage(i, 6*(box-1)+5) = E(5);
            tensorstorage(i, 6*(box-1)+6) = E(6);

        end
    end

    length(datamat)

    disp('To save results to a spreadsheet, type:');
disp('xlswrite(''(filename).xls'',tensorstorage,''(sheetname)'',''(range)'')'
);
```

Matlab Code – Resistivity Calibration for Strain

```
    % read ligament results and calibrate
    close all
    clear all
    clc

    data = xlsread('data_summary.xls','sheet1','D4:E969');
    strain=data(:,2);
    resistivity=data(:,1);
    fun=@(a) sum(abs(strain-(a(1)*(resistivity-a(4)).^a(2)-a(3))));
    a=fminsearch(fun,[3.159496502323236e+000    -1.189835542644368e+000    -
6.678384896561859e-002-.5                                                  -
5.456134370135228e+000],optimset('MaxFunEvals',1e6));
    strain_cal1=a(1)*(resistivity-a(4)).^a(2)-a(3);
    figure
    plot(strain,'k')
    hold on
    plot(strain_cal1,'r.')
    title('Actual and measured strain','FontSize',14)
    xlabel('Frame (10 Hz)','FontSize',14)
    ylabel('Strain (in/in)','FontSize',14)
    meanerror1=sum(abs(strain-a(1)*(resistivity-a(4)).^a(2)-
a(3)))/length(strain);
    relmeanerror1=sum(abs((strain-a(1)*(resistivity-a(4)).^a(2)-
a(3))./strain))/length(strain);


    data2 = xlsread('data_summary.xls','sheet1','H4:I1042');
    strain2=data2(:,2);
    resistivity2=data2(:,1);
    strain_cal2=a(1)*(resistivity2-a(4)).^a(2)-a(3);
    figure
    plot(strain2,'k')
    hold on
    plot(strain_cal2,'b.')
    title('Actual and measured strain','FontSize',14)
```

```
      xlabel('Frame (10 Hz)','FontSize',14)
      ylabel('Strain (in/in)','FontSize',14)
      meanerror2=sum(abs(strain2-a(1)*(resistivity2-a(4)).^a(2)-
a(3)))/length(strain2);
      relmeanerror2=sum(abs((strain2-a(1)*(resistivity2-a(4)).^a(2)-
a(3))./strain2))/length(strain2);


      data3 = xlsread('data_summary.xls','sheet1','L4:M1023');
      strain3=data3(:,2);
      resistivity3=data3(:,1);
      strain_cal3=a(1)*(resistivity3-a(4)).^a(2)-a(3);
      figure
      plot(strain3,'k')
      hold on
      plot(strain_cal3,'g.')
      title('Actual and measured strain','FontSize',14)
      xlabel('Frame (10 Hz)','FontSize',14)
      ylabel('Strain (in/in)','FontSize',14)
      meanerror3=sum(abs(strain3-a(1)*(resistivity3-a(4)).^a(2)-
a(3)))/length(strain3);
      relmeanerror3=sum(abs((strain3-a(1)*(resistivity3-a(4)).^a(2)-
a(3))./strain3))/length(strain3);
```